Chemical Engineering Journal 530 (2026) 173423

Contents lists available at ScienceDirect

Chemical Engineering Journal

journal homepage: www.elsevier.com/locate/cej

Structural deactivation mechanisms of zeolite-supported magnesium chloride with water: Ammonia sorption stability for intensified scalable hydrogen storage

Aleksandra Zamljen [a,b], Anže Prašnikar [a], Alen Vizintin [c], Matej Huš [a,d], Blaž Likozar [a,*]

[a] Department of Catalysis and Chemical Reaction Engineering, National Institute of Chemistry, Hajdrihova 19, 1001, Ljubljana, Slovenia
[b] Faculty of Chemistry and Chemical Technology, University of Ljubljana, Večna pot 113, 1001, Ljubljana, Slovenia
[c] Department of Materials Chemistry, National Institute of Chemistry, Hajdrihova 19, 1001, Ljubljana, Slovenia
[d] Association for Technical Culture of Slovenia (ZOTKS), Zaloška 65, 1000, Ljubljana, Slovenia

ARTICLE INFO

Keywords:
Metal halides
ammonia separation
Competitive absorption
Moisture stability
Sorption capacity
Green energy

ABSTRACT

$MgCl_2$ is a highly effective ammonia sorbent due to its strong and reversible interaction with ammonia, making it attractive for storage and separation applications. However, its strong tendency to absorb moisture presents a major practical challenge, and the effects of water exposure on supported $MgCl_2$ remain poorly understood. This work investigates $MgCl_2$ supported on ultra-stable Y zeolite, quantitatively linking material exposure to relative humidity with ammonia sorption capacity. FTIR and XPS analyses show that water exposure decreases ammonia uptake capacity by forming oxygenated Mg species such as MgO and MgOHCl, which replace active $MgCl_2$ sites. Pre-ammoniation does not prevent water uptake, as NH_3 displacement by H_2O is energetically favourable. DFT calculations also reveal that ligand exchange is thermodynamically more favourable than water intercalation, providing new mechanistic insight into material degradation. Furthermore, temperature-programmed desorption results show that simultaneous exposure to NH_3 and H_2O alters the coordination environment of the Mg^{2+} centre, reducing the stability of ammonia complexes. Cycling experiments, along with XRD, demonstrate that while thermal treatment alone does not alter the $MgCl_2$ structure, repeated ammonia absorption and desorption induce irreversible changes. These include the formation of defect-rich crystalline domains, which reduce sorption capacity over time. High-temperature dynamic sorption experiments show that although sorption capacity decreases at higher temperatures, $MgCl_2$/USY retains a measurable capacity of up to 65 mg/$g_{sorbent}$ at 300 °C and 8 bar. This indicates that the sorbent may still operate under integrated ammonia synthesis-separation conditions. This study provides the first quantitative, mechanistic understanding of moisture- and dry NH_3 cycling-induced degradation of supported $MgCl_2$ sorbents, defining operational conditions for their integration into ammonia synthesis-separation process.

1. Introduction

Ammonia is considered one of the key chemicals in our society due to its widespread use. In the 20th century, ammonia revolutionised agriculture by enabling large-scale production of nitrogen-based fertilisers, which fuelled rapid population growth [1]. In recent years, it has also gained recognition as an energy vector, especially as a means of indirect hydrogen storage, owing to its high gravimetric (17.8 wt%) [2] and volumetric hydrogen density (11.5 MJ/L) [3]. Today, ammonia plays a dual role: it remains a key fertiliser feedstock and also serves as a high energy density vector, making it one of the most important processes in the chemical industry. However, traditional Haber-Bosch synthesis remains highly energy-intensive [4], largely due to the high energy demand associated with cooling, condensing, and recycling unreacted nitrogen and hydrogen [5,6].

The global drive towards decarbonization has prompted significant innovation in green ammonia production [7], with new technologies aiming to replace conventional fossil fuel-based methods with renewable pathways [8]. The concept of small, decentralized plants for on-site ammonia production has recently gained significant attention [9], as these systems can utilize sustainable feedstocks such as water and air, enabling ammonia production without CO_2 emissions [10]. Yet,

* Corresponding author.
E-mail address: blaz.likozar@ki.si (B. Likozar).

https://doi.org/10.1016/j.cej.2026.173423
Received 15 December 2025; Received in revised form 23 January 2026; Accepted 24 January 2026
Available online 30 January 2026

downscaling ammonia synthesis is often economically challenging [11], since achieving higher single-pass conversion typically requires high pressures and subzero condensation. The process therefore requires costly compressors, high-pressure vessels, and refrigeration systems [12].

One promising strategy to lower energy and cost penalties is the use of ammonia-absorbing materials. Ammonia can be more effectively removed by solid sorbents than by condensation [12], shifting the reaction equilibrium, enhancing conversion, and possibly enabling a more compact and flexible smaller-scale ammonia plants [13]. This approach is particularly attractive given the kinetic limitations in iron and ruthenium catalysts for ammonia synthesis, where the equilibrium removal of ammonia is one of the most effective routes to improve conversion [14,15]. The performance of these sorbents depends on their capacity, selectivity, and sorption kinetics [10,16]. Among solid ammonia sorbents, metal halides have emerged as leading candidates for this role, due to their high sorption capacity, reversibility [17], high selectivity over hydrogen and nitrogen [17], and the ability to remove ammonia at elevated temperatures [18]. To enhance performance, metal halides are often supported on porous materials with high surface area, for instance zeolites [18], activated carbon [19], MOFs [20] and COFs [21] to improve kinetics and material stability.

Although metal halides such as $MgCl_2$ are at present the most promising scalable high temperature ammonia sorption materials used for in-situ ammonia removal [13], their strong tendency to absorb moisture creates a significant practical hurdle. Even small amounts of water can trigger partial hydrolysis upon heating, causing the formation of oxide-containing compounds like MgOHCl. The latter further degrades to HCl and MgO, which irreversibly alters the material's structure and reduces the number of available coordination sites for ammonia binding [22]. Since completely avoiding humidity is nearly impossible in real operating conditions, it is important to mitigate moisture-induced deactivation to maintain reliable sorbent performance [23]. This becomes especially important in applications such as cyclic ammonia synthesis-sorption, ammonia heat pumps, and gas purification, where contact with humid gas streams is inevitable. In industrial ammonia synthesis loops, minor amounts of H_2O, CO_2, O_2, and CO may be present and can act as reversible poisons for ammonia synthesis catalysts [24]. Among these, H_2O is particularly relevant due to its formation during the catalyst reduction and the hygroscopic nature of $MgCl_2$. While CO_2 could theoretically react with NH_3, its concentration in the synthesis loop is typically negligible under standard operating conditions [24–26].

While the hydration and hydrolysis of $MgCl_2$ are well documented [27], previous studies have primarily focused on bulk $MgCl_2$ chemistry and have not quantitatively linked moisture exposure to ammonia sorption performance in supported $MgCl_2$ systems. In this work, we investigate USY-supported $MgCl_2$ as an ammonia sorbent, quantifying the effect of water on ammonia sorption capacity and identifying the structural and chemical changes responsible for performance loss. We also investigate the influence of pre-ammoniation of the sorbent on material stability and evaluate the cyclic stability of the material under dry conditions, revealing the formation of irreversible defect-rich phases after repeated cycles. Furthermore, density functional theory (DFT) calculations provide insight into competitive NH_3 and H_2O binding, clarifying the mechanisms of ligand exchange. Finally, sorption capacities are measured across a range of temperatures and pressures to assess sorbent performance under conditions relevant to industrial ammonia synthesis. These results provide valuable insight into the design of robust, high-performance ammonia sorbents for sustainable ammonia-based energy and chemical processes.

2. Methods

2.1. Sources of materials

For BT and NH_3-TPD measurements, a gas mixture of 9.88 vol% NH_3 in He (5.0, Messer) was used. Prior to breakthrough analysis, the reactor was purged with helium gas (5.0, Messer). Ethanol absolute anhydrous ($\geq$ 99.5% purity, CAS No. 64–17-5) from Carlo Erba was used for the synthesis. Magnesium chloride anhydrous ($\geq$ 98% purity, CAS No. 7786-30-3) was obtained from Sigma Aldrich.

2.2. Material preparation

Prior to synthesis, the supports were pretreated overnight at 400 °C, while magnesium chloride was used as received. The wet impregnation method was used to synthesise the supported metal halide in a round-bottom, two-necked flask equipped with a condenser under an inert argon atmosphere. A total of 200 mL of anhydrous ethanol was added to 10 g of magnesium chloride and heated in an oil bath until ethanol reached its boiling point. The solution was stirred under total reflux for 1 h. While maintaining the temperature, 10 g of support (ultra-stable Y zeolite – USY) was then added to the flask. The resulting suspension was stirred for a further 3 h under the same conditions before the solvent was vacuum-evaporated. The impregnated material was then heated to 400 °C in the inert atmosphere and stored under inert conditions.

2.3. Sorbent characterisation

The samples were transferred, ground to powder, and prepared in a glovebox for all analyses. For the X-ray diffraction (XRD) analyses, samples were placed in the sample holder and covered with Kapton foil. The analyses were performed using a PANalytical X'Pert Pro MPD instrument with a Cu Kα1 radiation source. XRD patterns were obtained over a range of 1° to 80° or 90° 2θ, using a measurement increment of 0.033° and a step time of 100 s.

Scanning electron microscopy (SEM) and energy dispersive spectroscopy (EDS) were performed using a SUPRA35 VP scanning electron microscope (Carl Zeiss) equipped with an Inca 400 EDS detector (Oxford Instruments). The samples were placed on conductive carbon tape, which had been previously secured to a metal support. The samples were prepared under an inert atmosphere and vacuumed prior to analysis. SEM analysis was carried out at 1 kV (EHT) with an aperture size of 30.00 μm, and EDS analysis was conducted at three different locations on the sample, using 20 kV and an aperture size of 120 μm for 1 min.

N2 physisorption was used to determine the specific surface area by the Brunauer-Emmett-Teller (BET) method and pore size distributions by the Tarazona NLDFT method, assuming cylindrical geometry, based on N2 adsorption data. Measurements were performed on a Belsorp (Microtrac) at 77 K after pretreatment at 300 °C overnight under vacuum.

The metal halide loading was determined using inductively coupled plasma optical emission spectrometry (ICP-OES) with a Varian 715 ES ICP Optical Emission Spectrometer. The samples were weighed under an inert atmosphere before analysis.

Fourier-transform infrared spectroscopy (FTIR) measurements were carried out using a Spectrum 3 (Perkin Elmer). Spectra were collected over the range 4000–450 cm^{-1}, with 32 scans averaged for each sample. FTIR spectra of $MgCl_2$, $MgCl_2$/USY, NH_3-pretreated $MgCl_2$/USY, and USY were recorded after different exposure times to air at 30% relative humidity. For the NH_3-treated samples, pretreatment was conducted at 25 °C under a flow of 10% NH_3/He until saturation was reached.

X-ray photoelectron spectroscopy (XPS) was performed using a Versa Probe 3 AD (Physical Electronics, Chanhassen, U.S.A.) with focused monochromatic Al Kα radiation at 15 kV and 13.3 mA. Sample preparation for XPS measurements was carried out inside an argon-filled glovebox (0.1 ppm O_2 and H_2O). The powdered samples were placed

on non-conductive double-sided Scotch tape at the centre of the XPS holder. The samples were transferred into the XPS introduction chamber using a transfer vessel without air exposure, thus protecting them from water contamination. The spectrometer was calibrated using the internal standard Au 4f7/2 at 83.99 eV. The analysis chamber pressure was approximately 10^{-8} Torr. Spectra were obtained by scanning a 1 × 1 mm area. High-resolution spectra were measured at 27 eV pass energy with a step size of 0.05 eV. Peak analysis was performed by fitting the spectra using a linear combination of Gaussian and Lorentzian component curves after Shirley background subtraction.

2.4. Sorption tests

To determine the amounts of absorbed and desorbed ammonia, breakthrough experiments (BT) and ammonia temperature-programmed desorption experiments (NH3-TPD) were performed using a Belcat II (Microtrac). Powdered samples were placed in a quartz reactor, and the gas concentration was monitored with a thermal conductivity detector (TCD). Simultaneously, a quadrupole mass spectrometer (Belmass II) was used to confirm the absence of impurities. An ammonia partial pressure of 0.1 bar was used in the experiments. Additional details are provided in the Supporting Information (Fig. S1). A Constant Climate Chamber (CPR 240 Premium, VWR) was used to control temperature and humidity during humidity exposure experiments.

2.5. High-temperature tests

Ammonia BT experiments were conducted using a Micromeritics flow reactor (FR 200). Approximately 300 mg of the powdered sample was loaded into the reactor, with quartz wool placed at both ends of the column to hold the absorbent material in place. A thermocouple, positioned directly in the sample, was used to monitor the temperature, while gas concentrations were measured with a microGC (Inficon). All samples were handled under an argon atmosphere to prevent moisture contamination. A gas mixture containing 10 vol% NH3 in helium was used for the experiments, with a constant flow rate of 30 SCCM. Experiments were conducted at three different temperatures (50, 150, 300 °C) and pressures (1, 5, 8 bar), corresponding to NH3 partial pressures of 0.1, 0.5, and 0.8 bar. For each temperature, the same sample was measured sequentially at 1, 5, and 8 bar. The pretreatment and regeneration of the sample were performed at 400 °C. A blank test was conducted with the reactor filled with inert material (SiC) at 1 bar.

2.6. Computational methods

For theoretical calculations, density functional theory was employed using the plane-wave approach, as implemented in VASP 6.3.1 [28–32]. The structures were described with a plane-wave basis set, the revised PBE (RPBE) [33] exchange-correlation functional, and the projector-augmented-wave method. An energy cutoff of 500 eV, Gaussian smearing of 0.03 eV, and a spin-restricted description of the wave function were used. Dispersion interactions were included using the empirical Grimme D3 correction [34]. Dipole corrections were not required, as no slab structures were studied. For $MgCl_2$ and $MgCl_2 \cdot 2\ H_2O$, 2 × 2 × 2 supercells were constructed, with the Brillouin zone sampled using a 1 × 1 × 3 K-point mesh. The unit cell of $MgCl_2 \cdot 6\ H_2O$ is sufficiently large that a single unit cell, sampled at the Γ point, was adequate. Isolated molecules (H_2O and NH_3) were computed in a large (20 Å × 20 Å × 20 Å) unit cell.

Initially, we optimised the canonical, experimentally determined unit cells of $MgCl_2$, $MgCl_2 \cdot 2\ H_2O$, and $MgCl_2 \cdot 6\ H_2O$, as shown in Table 1. The DFT-obtained values differ from the experimental values by 0.6–2.1%. For $MgCl_2{\cdot}2\ H_2O$ and $MgCl_2{\cdot}6\ H_2O$, where non-ionic interactions play an important role, the dispersion correction slightly overestimates the values, while for purely ionic $MgCl_2$, the predicted unit cell is slightly too large, as expected. The energetics of ammonia and water substitution were computed relative to isolated NH_3 and H_2O.

3. Results and discussion

$MgCl_2$ is an effective ammonia absorbent, but its practical application requires a porous support that enables high dispersion while maintaining structural stability. USY zeolite was selected as a support due to its highly porous structure and large pore volume, which enable high $MgCl_2$ loading and uniform salt dispersion. Its high thermal and chemical stability ensure structural stability during ammonia absorption at high temperatures and pressures. The interconnected pore network promotes efficient gas diffusion and mass transport. Furthermore, USY 500 (Si/Al = 500) has a relatively hydrophobic framework, which helps limit excessive water uptake by the support. A schematic representation of $MgCl_2$/USY synthesis and its reaction with ammonia is given in Fig. S3.

The actual loading of $MgCl_2$ on USY support was determined to be 50.2 wt% by the ICP-OES analysis, which closely aligns with the targeted value of 50 wt% from the synthesis process. The XRD pattern of $MgCl_2$/USY in Fig. 1 shows low-intensity diffraction peaks of $MgCl_2$ at 15, 30.2, 35, and 50.5°2θ after thermal treatment at 400 °C, indicating that $MgCl_2$ is present as a separate crystalline phase and is highly dispersed within the support's porous structure. The presence of distinct $MgCl_2$ and USY phases indicates that $MgCl_2$ is stabilized mainly by electrostatic interactions and physical confinement. This is consistent with the BET analysis, discussed below, which suggests that $MgCl_2$ blocks the support's pores upon impregnation.

N_2 physisorption isotherms of zeolite USY and $MgCl_2$/USY are shown in Fig. 2. BET surface area and total pore volume of zeolite USY are 850 m^2/g and 0.5 cm^3/g, respectively. The BET surface area decreased to 427 m^2/g after zeolite USY was impregnated with $MgCl_2$, while total the pore volume also decreased to 0.4 cm^3/g. The significant decrease in BET surface area after impregnation results from high $MgCl_2$ loading, which causes pore blockage and reduces the accessibility of the support [35,36]. Similar effects have been reported for salt-confined porous

Table 1
Comparison of experimentally determined and computationally optimised unit cell parameters of different $MgCl_2$ structures.

	Source	a	b	c	α	β	γ
$MgCl_2$	Exp. (ICDD: 04–008-7748)	3.6363	3.6363	17.6663	90°	90°	120°
$MgCl_2$	Computationally (this work)	3.6587 (+0.6%)	3.6587 (+0.6%)	17.7756 (+0.6%)	90°	90°	120°
$MgCl_2$•2 H_2O	Exp. (ICDD: 04–009-8931)	8.1810	8.2067	3.7550	90°	90°	90°
$MgCl_2$•2 H_2O	Computationally (this work)	8.1123 (−0.9%)	8.1384 (−0.9%)	3.7237 (−0.9%)	90°	90°	90°
$MgCl_2$•6 H_2O	Exp. (ICDD: 04–010-3690)	10.1899	10.1899	10.1899	90	90°	90°
$MgCl_2$•6 H_2O	Computationally (this work)	9.9942 (−2.1%)	9.9942 (−2.1%)	9.9942 (−2.1%)	90	90°	90°

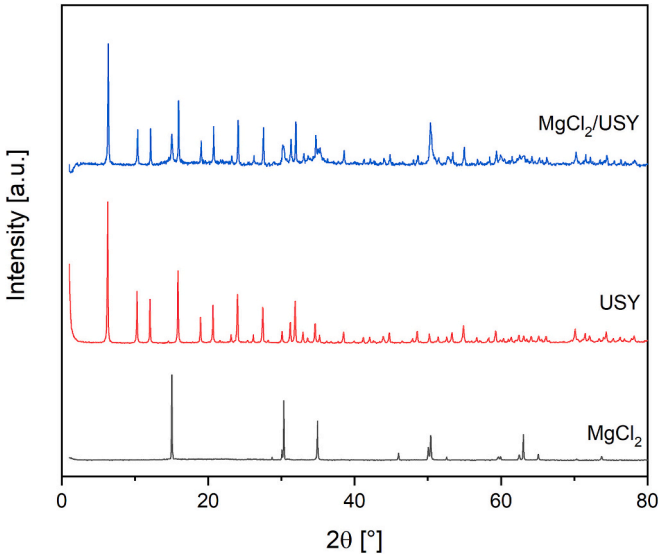

Fig. 1. XRD patterns of $MgCl_2$, USY and $MgCl_2$/USY.

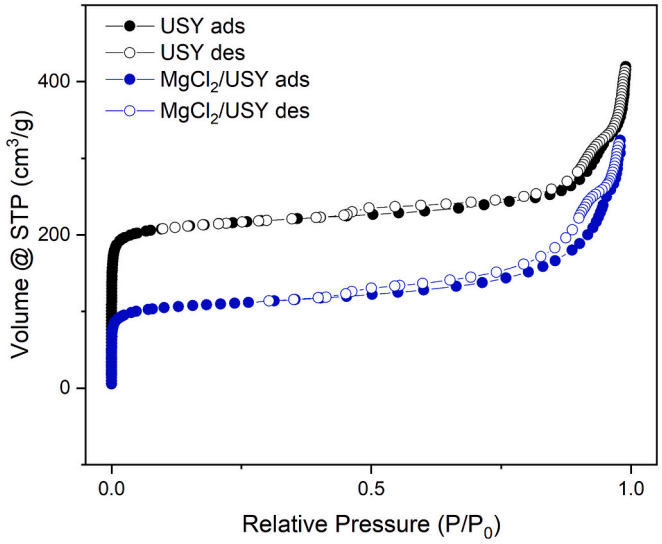

Fig. 2. N_2 adsorption/desorption isotherms of $MgCl_2$/USY and USY.

sorbents, where sorption performance is strongly affected by salt loading and its dispersion within the pore network. Previous studies have shown that variations in loading can directly affect gas sorption performance in metal salt loaded porous supports [37]. Excessive salt loading leads to reduced porosity [36]. The pore size distribution shows the large majority of the pores exhibit a size of around 1 nm (Fig. S4).

Pores are clearly visible on the surface of the characteristic FAU morphology of the USY zeolite (Fig. 3). $MgCl_2$ particles are dispersed over the surface of the USY support, as observed from SEM analysis, and within the pores of the support, as determined by BET analysis. Furthermore, a uniform spatial distribution of $MgCl_2$ over the USY support was observed from EDS elemental mapping (Fig. S5). Carbon was detected because conductive carbon tape was used to attach the material to the sample holder.

3.1. Humidity-driven chemical transformation

3.1.1. Influence of humidity on sorption capacity

Moisture sensitivity is an important factor in determining the reliability of sorbents in practical environments. To evaluate the effect of moisture exposure, sorption tests were performed on the sorbent after treatment under an inert atmosphere or exposure to air at controlled humidity levels (30, 50, 75% RH) at 25 °C. For the latter, samples were placed in a constant climate chamber to maintain a constant relative humidity. Exposure times were varied (0, 2, and 4 h), after which the sorption capacity was measured under the same conditions and compared to the unexposed sorbent. Breakthrough experiments were conducted at 25 °C, while desorption was carried out by heating the sample to 400 °C. The results (Fig. 4, Tables S1 and S2) reveal a significant decline in ammonia absorption capacity following moisture

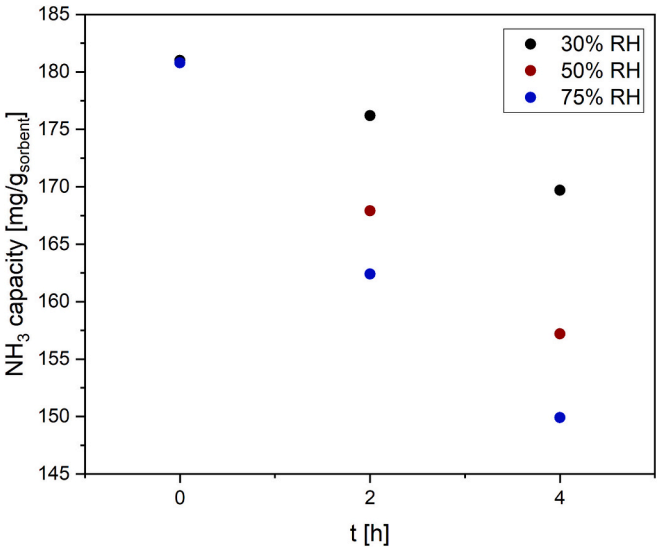

Fig. 4. Ammonia capacity of $MgCl_2$/USY at different time exposure to moisture (30, 50, 75% RH) at 25 °C.

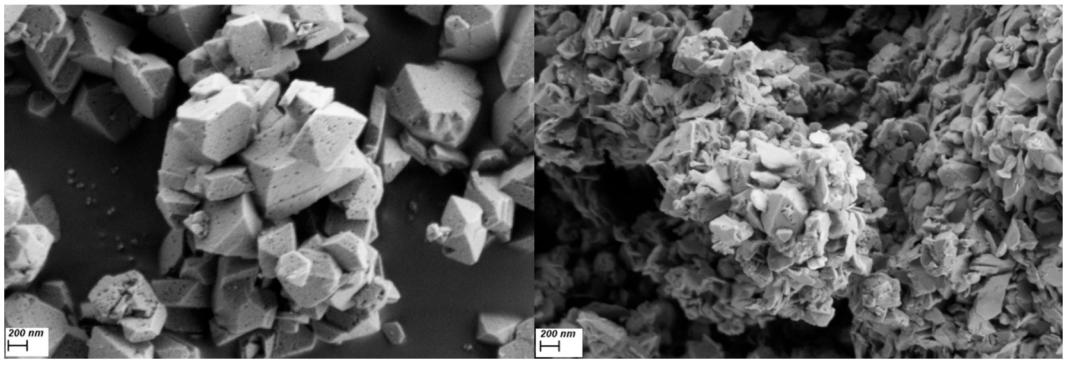

Fig. 3. SEM images of USY (left), and $MgCl_2$/USY (right) at 50 k magnification.

exposure: $MgCl_2$/USY exhibited a decrease in capacity, which became more pronounced at higher relative humidity levels. The observed loss in ammonia capacity can be attributed to the formation of oxygen-containing species.

The extent of oxygen species formation on the surface of $MgCl_2$/USY was evaluated using XPS. Recent work by Skaanvik et al. [38] clarifies how to reliably distinguish between $MgCl_2$, MgOHCl, $Mg(OH)_2$, and MgO species using developed O 1s curve-fitting procedures, even when their Mg *2p* signals overlap significantly. This confirms that the oxygen species detected in our samples accurately reflect their chemical state, while acknowledging that XPS is inherently surface-sensitive and does not detect species located within the pores of the USY framework. As a result, XPS is used here to track qualitative chemical transformations induced by moisture exposure, rather than to quantitatively determine bulk phase fractions.

The Cl 2p high-resolution XPS spectrum (Fig. 5b) shows that the $MgCl_2$/USY sample stored under an inert atmosphere contains only $MgCl_2$, confirming the absence of contaminants. Similarly, the O 1s orbital (Fig. 5a) shows only oxygen originating from the zeolitic framework of USY. In contrast, samples exposed to 30% RH and 75% RH for 4 h exhibit a clear MgO contribution. Both samples also show the presence of $Mg(OH)_2$ and MgOHCl species, with higher relative peak areas observed for the sample exposed to 75% RH (Tables S3 and S4), indicating more extensive surface hydrolysis under exposure to higher moisture levels. These oxygen-containing phases appear because $MgCl_2$ is highly hygroscopic and rapidly forms hydrated salts when exposed to moisture. The formation of MgOHCl is also confirmed in the Cl *2p* spectrum (Fig. 5b). When these hydrates ($MgCl_2 \bullet xH_2O$) are heated, even under an inert atmosphere such as N_2 or Ar, they do not simply dehydrate back to anhydrous $MgCl_2$. Instead, a hydrolysis pathway is favoured [27]:

$$Mg(H_2O)Cl_2 \rightleftharpoons MgOHCl + HCl \quad (1)$$

which further proceeds as:

$$MgOHCl \rightleftharpoons MgO + HCl \quad (2)$$

As reported by Huang et al. [27], R1 occurs up to approximately 235 °C, while R2 proceeds at around 415 °C. XPS analyses of moisture-exposed samples show the presence of MgOHCl, $Mg(OH)_2$, and MgO species, as R2 partially proceeds at 400 °C, supporting evidence of a moisture-driven hydrolysis pathway. Importantly, the emergence of Mg oxygenated species coincides with the experimentally observed decrease in ammonia capacity (Fig. 4). These thermodynamically stable residues do not form coordination complexes with ammonia, showing a direct mechanistic link between surface phase transformation and the loss of ammonia uptake. Therefore, any partial decomposition of $MgCl_2$ to MgO results in a significant reduction in ammonia capacity.

3.1.2. *Pre-ammoniation before exposure to humidity*

Given the potential for pre-ammoniation to improve the stability of $MgCl_2$ sorbent during handling and storage, additional sorption experiments were conducted to compare the moisture stability of non-ammoniated and ammoniated sorbents. The objective was to determine whether pre-ammoniated sorbents retain ammonia after exposure to a humid environment, assuming that water cannot replace ammonia as a ligand. For this purpose, the sample underwent one cycle of ammonia absorption, forming $Mg(NH_3)_6Cl_2$ without subsequent desorption, after which it was exposed to a controlled atmosphere at 75% relative humidity. A second sample underwent the same initial absorption cycle, followed by ammonia desorption before exposure to humidity. Both materials were exposed to the humid environment for 3 h and then tested over five additional cycles of ammonia absorption and

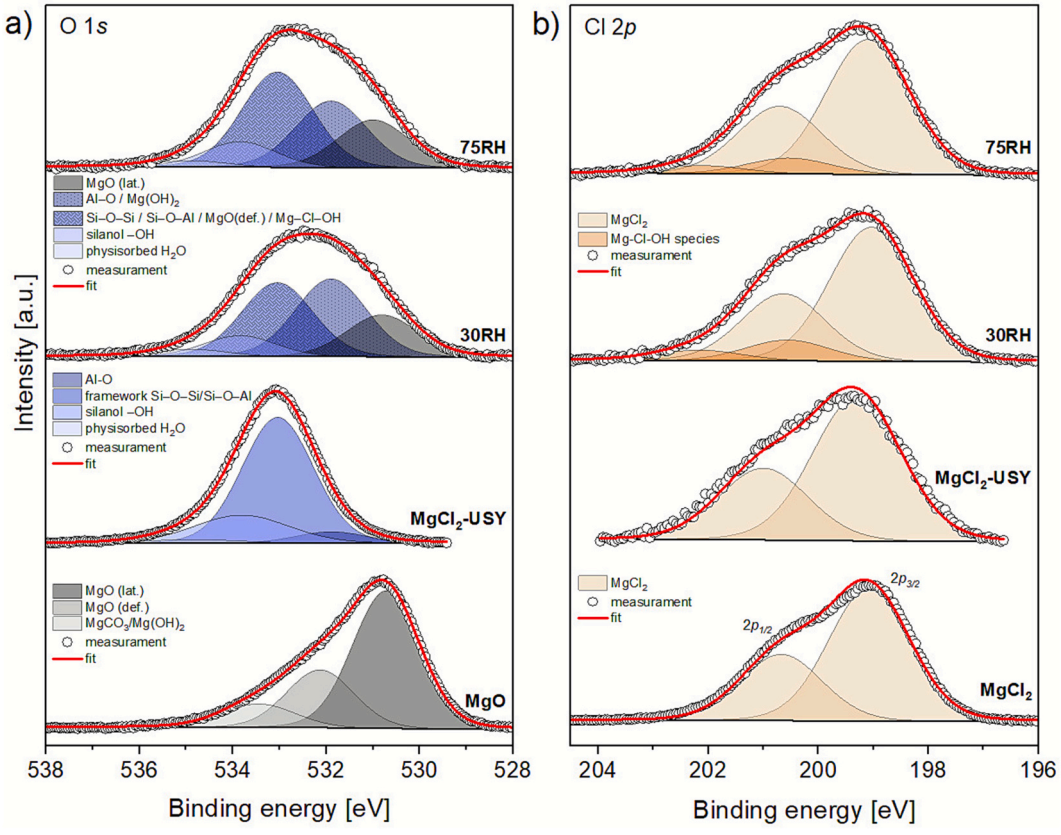

Fig. 5. High-resolution XPS spectra of a) O 1*s* and b) Cl 2*p* orbitals of $MgCl_2$/USY sample in the inert atmosphere, sample exposed to 30 and 75% RH, and bulk MgO and $MgCl_2$ for comparison.

desorption. Regeneration during cycling was performed with a 10 °C/min ramp up to 400 °C, holding this temperature for 20 min, before cooling the sample for the next absorption. The measurement is explained in detail in Fig. S2, and the ammonia breakthrough curves used to calculate sorption capacities are shown in Fig. S7.

Fig. 6 reveals two different degradation routes: a humidity-driven chemical transformation and a dry ammonia sorption-driven route. The reduced ammonia capacity between the first and second cycles can be attributed to the formation of new oxygen species resulting from exposure to humidity, as explained by the XPS analysis (Fig. 5). In Fig. 6, it can be seen that the subsequent cycles (when the water is desorbed, and the material is cycled under an inert atmosphere), the capacity drop in water-exposed materials follows the trend of the unexposed sample. This indicates that the $MgCl_2$ structural instability alone is responsible, which is further discussed in Section 3.2.1.

Contrary to expectations, the results (Fig. 6, Tables S1 and S2) show that the pre-ammoniated sample exhibited a more pronounced decline in ammonia sorption capacity than the non-ammoniated sample after moisture exposure. This suggests that the presence of coordinated ammonia may facilitate interaction with water. In humid air, water has a very strong affinity for Mg^{2+} sites, as thoroughly investigated by Tavani et al. [39] Their ambient-pressure soft X-ray absorption spectroscopy demonstrated that water binds strongly and selectively to under-coordinated Mg^{2+} surface sites, forming a distinct hydrated species that remains stable even at elevated temperatures. The hydration of $MgCl_2$ is both energetically favourable and not easily reversed, indicating that water can effectively displace pre-coordinated ligands such as NH_3. These findings show that pre-ammoniation is ineffective for mitigating humidity sensitivity under humid conditions and should not be relied upon for handling or operation.

Our computational results (vide supra) indicate that in humid air, H_2O can replace NH_3 bound to $MgCl_2$, as the Mg^{2+}–H_2O interaction is comparably strong to the Mg^{2+}–NH_3 interaction, making hydration energetically accessible. In humid air, the high relative concentration of H_2O further promotes ligand exchange. Energetically, ligand exchange is more favourable than H_2O intercalation. In contrast, pure $MgCl_2$ exhibits stronger intrinsic interactions between Mg^{2+} and Cl^-, which could slow water coordination relative to ligand exchange in the ammoniated phase.

Fig. 7a shows the FTIR spectrum of anhydrous $MgCl_2$ at different exposure times to air at 30% relative humidity. The FTIR spectrum displays a strong absorption band around 450–500 cm^{-1}, corresponding to the Mg—Cl stretching vibration characteristic of metal halide salts. A low-intensity absorption band at 1638 cm^{-1} can be attributed to the O—H bending of absorbed water [40], and its intensity increases significantly over time due to H_2O coordination to $MgCl_2$. Similarly, the intensity of the broad absorption band around 3200–3500 cm^{-1} increases over time due to the O—H stretching vibration of water molecules and hydrogen bonding among water molecules.

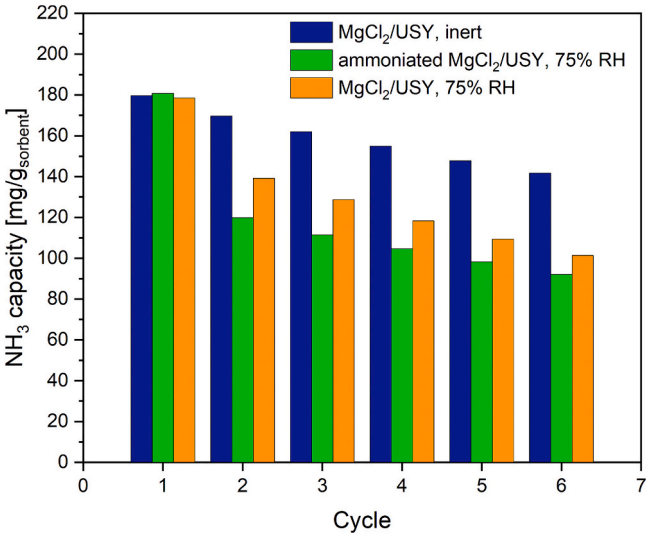

Fig. 6. Ammonia capacity over 6 cycles for $MgCl_2$/USY unexposed to moisture, $MgCl_2$/USY exposed to moisture (75% RH at 25 °C for 3 h) after ammonia absorption, and $MgCl_2$/USY exposed to moisture after ammonia absorption and subsequent desorption.

In the initial spectrum of $MgCl_2$/USY (Fig. 7c), there are no broad bands attributable to water. Over time, the band intensity at 1638 cm^{-1} increases, which is attributed to the O—H bending of absorbed water. A broad absorption band around 2700–3750 cm^{-1} is also observed, due to the O—H stretching vibration of water molecules, indicating coordination of water molecules to $MgCl_2$. The FTIR spectrum of NH_3-pretreated zeolite USY (Fig. 7b) shows bands around 1084 cm^{-1}, attributed to the asymmetric stretching vibration of Si–O–Si, while no bands corresponding to O—H vibration are observed, indicating that no water is absorbed by the zeolite over time. The observed bands in the FTIR spectra of $MgCl_2$/USY therefore arise solely from H_2O coordination to $MgCl_2$.

Compared to unpretreated $MgCl_2$/USY, the NH_3-pretreated sample (Fig. 7d) shows a band at 1410 cm^{-1} corresponding to N—H vibration [41], which proves the chemical coordination of ammonia to $MgCl_2$, as no such band is observed in NH_3-pretreated USY zeolite. During exposure to air, the band for water at 1638 cm^{-1} increases relative to the band corresponding to ammonia. The rate of increase of this band is comparable for both non-ammoniated and ammoniated $MgCl_2$/USY, suggesting that under the studied conditions, ammoniation does not significantly change the kinetics of water contamination. However, even after several hours, ammonia remains present in the system, indicating that water does not replace it, or only partially replaces it. This suggests that water interacts with ammonia through hydrogen bonding. A similar effect is observed at 75% RH (Fig. S6).

Temperature-programmed desorption (TPD) measurements show that the presence of water significantly affects ammonia absorption and desorption behaviour. Simultaneous exposure to NH_3 and H_2O can lead to the formation of mixed hydrates or ammoniates, affecting both the structural stability and sorption capacity of the metal halide. As observed in Fig. 8b, the $MgCl_2$/USY sample treated under inert conditions exhibits three well-defined NH_3 desorption peaks, corresponding to well-known specific desorption equations:

$$Mg(NH_3)_6Cl_2(s) \rightleftharpoons Mg(NH_3)_2Cl_2(s) + 4NH_3(g) \quad (3)$$

$$Mg(NH_3)_2Cl_2(s) \rightleftharpoons Mg(NH_3)Cl_2(s) + NH_3(g) \quad (4)$$

$$Mg(NH_3)Cl_2(s) \rightleftharpoons MgCl_2(s) + NH_3(g) \quad (5)$$

Fig. 8c shows reduced ammonia desorption peak intensities, indicating a lower ammonia uptake capacity after the water exposure, consistent with the results in Fig. 6. Additionally, a shift in the last two desorption peaks is observed. The pre-ammoniated sample exposed to 75% RH for 3 h (Fig. 8a) shows a noticeable shift in the last two desorption peaks. This indicates reduced desorption energy and therefore weaker ammonia binding. The results suggest that moisture exposure alters the coordination environment of $MgCl_2$, reducing the stability of the ammonia complexes. This is consistent with the findings of Tavani et al., who reported that hydration causes a measurable change in Mg K-edge spectral features, indicating the formation of a new coordination environment [39].

Comparable behaviour has also been reported in studies of NH_3 absorption in metal-organic frameworks (MOFs) by Tan et al. [42], where H_2O displaces metal-coordinated ammonia as water concentration increases. Computational analysis has attributed this exchange process to a reduced kinetic barrier and a favourable energetic state resulting from the formation of metal clusters at metal sites and intermolecular hydrogen bonding between the metal-coordinated water and displaced

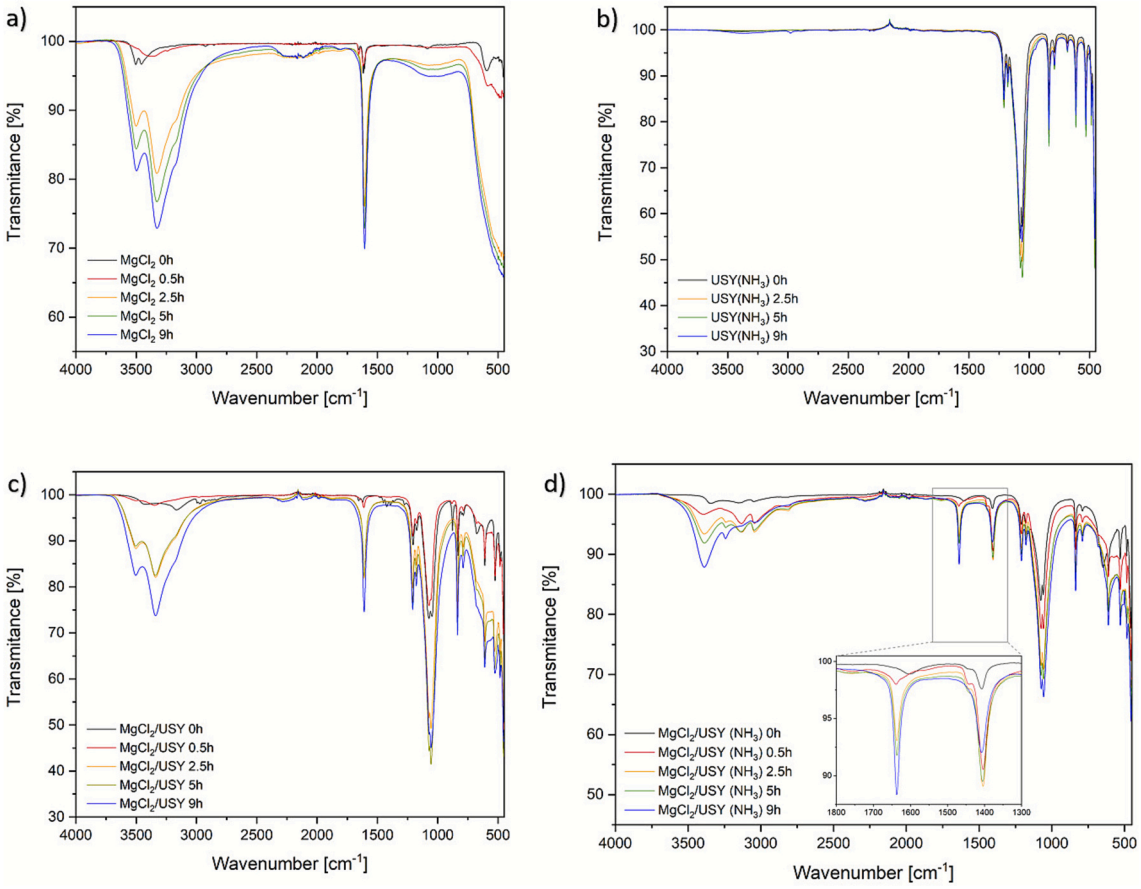

Fig. 7. FTIR spectra of a) $MgCl_2$, b) ammoniated USY, c) $MgCl_2$/USY, d) ammoniated $MgCl_2$/USY at different time exposure to air at 30% RH.

ammonia. Specifically, hydrogen bonding between water and coordinated ammonia weakens the metal–nitrogen interaction, facilitating ammonia displacement by reducing the kinetic barrier. A similar trend is observed in our FTIR spectra, where the intensity of the water band increases over time while the ammonia band remains present. This indicates that water is bound to ammonia through hydrogen bonding (Fig. 7d).

3.1.3. *Quantum chemical calculations*

We first analysed the energetics of the formation of $MgCl_2 \bullet 2\ H_2O$ and $MgCl_2 \bullet 6\ H_2O$, which are shown in Fig. 9. For the reaction $MgCl_2(s) + 2NH_3(g) \rightleftharpoons Mg(NH_3)_2Cl_2(s)$, the calculated energy change is −185 kJ mol-1 or − 0.96 eV per 1 NH_3. For the reaction $MgCl_2(s) + 6NH_3(g) \rightleftharpoons Mg(NH_3)_6Cl_2(s)$, the calculated energy change is −461 kJ mol-1 or − 0.80 eV per 1 NH_3. This is consistent with existing literature [43] and our experimental data.

To understand the binding of the ammonia molecule, Bader charge analysis was performed. In pure $MgCl_2$, the effective Bader charges are +1.66 for Mg^{2+} and − 0.83 for Cl^-. In $MgCl_2{\cdot}2\ H_2O$ and $MgCl_2{\cdot}6\ H_2O$, ammonia ligands donate a small amount of electron density, decreasing the charge on Mg^{2+} to +1.64 and + 1.63, respectively. Substituting one NH_3 for H_2O does not affect the charge on Mg^{2+}. However, when a ligand (NH_3) is removed, the charge on Mg^{2+} increases by +0.02. Differential charge density due to absorption of NH_3 is shown in Fig. 10.

We also calculated the energy required to remove one ammonia molecule from $MgCl_2 \bullet 2\ H_2O$ and $MgCl_2 \bullet 6\ H_2O$ in the limit of low defect concentration. This was achieved using large supercells, which contained 16 NH_3 molecules for $MgCl_2 \bullet 2\ H_2O$ and 24 NH_3 molecules for $MgCl_2 \bullet 6\ H_2O$·In $MgCl_2 \bullet 2\ H_2O$, removing one NH_3 requires 121.7 kJ mol^{-1}, while adding H_2O in its place releases 111.3 kJ mol^{-1}. Water can also intercalate into the structure without displacing NH_3, which requires 60.2 kJ mol^{-1} per water molecule.

In $MgCl_2 \bullet 6\ H_2O$, there are two distinct types of ammonia ligands, differing by their coordination site: two axial and four equatorial NH_3 per $MgCl_2$ unit. The energy required for their removal is similar, at 95.8 and 94.8 kJ mol^{-1}, respectively. Substituting them with a water molecule releases 90.3 and 91.7 kJ mol^{-1}, indicating that, relatively, water substitution proceeds more readily than in $MgCl_2 \bullet 2\ H_2O$. Interestingly, when two ammonia ligands are removed from the same Mg^{2+}, one equatorial and one axial NH_3 are removed, with a total energy change of +180.2 kJ mol^{-1} (90.1 kJ mol^{-1} per NH_3, showing that the second removal is slightly more favourable). In contrast, removing either two axial or two equatorial ligands requires 228.9 and 227.7 kJ mol^{-1}, respectively, which is less favourable. However, $MgCl_2 \bullet 6\ H_2O$ intercalates water molecules more easily than $MgCl_2 \bullet 2\ H_2O$, with an energy change of +18.5 kJ mol^{-1}.

3.2. *Dry ammonia cycling*

3.2.1. *Cycling stability and $MgCl_2$ structural changes*

A key limitation of magnesium chloride-based sorbents is their poor cyclic stability at high temperatures, which remains a challenge for practical application. The ammonia capacity of $MgCl_2$/USY under dry conditions decreases over cycling, as shown in Fig. 6. Different regeneration conditions were applied to determine whether longer regeneration times or higher regeneration temperature improve cycling stability. The results indicate that extending the regeneration time or increasing the regeneration temperature does not prevent the decrease in ammonia capacity over cycling (Fig. 11). BT and TPD curves of these measurements are presented in Figs. S8 and S9. Furthermore, FTIR and SEM-EDS experiments (Figs. S10-S12) conducted after cycling confirm the absence of nitrogen in the samples, showing that no ammonia

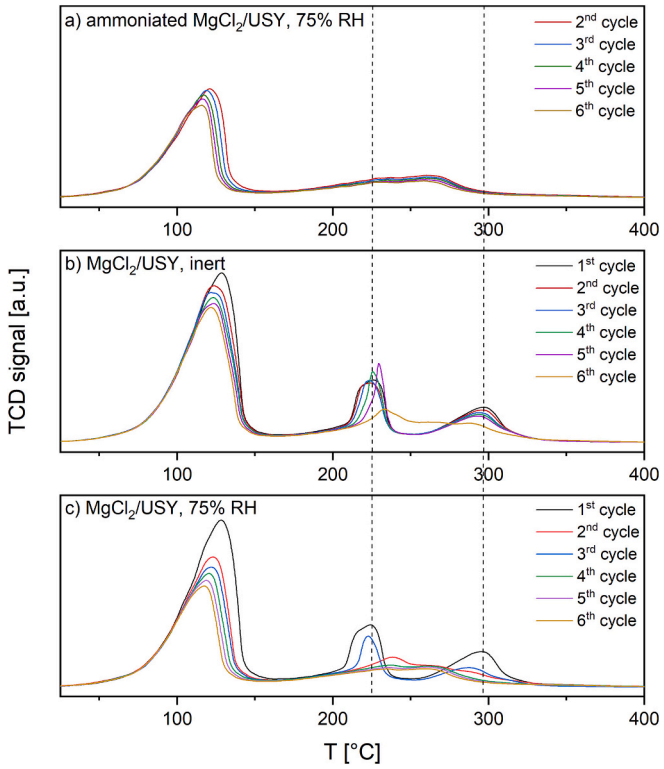

Fig. 8. TPD cyclic experiments of a) ammoniated $MgCl_2$/USY exposed to moisture for 3 h, b) $MgCl_2$/USY unexposed to moisture, c) non-ammoniated $MgCl_2$/USY exposed to moisture for 3 h.

remains in the sample after regeneration. This confirms that the capacity drop is not due to residual bound ammonia.

To determine the mechanism of material degradation during cycling under dry conditions, XRD patterns were recorded for $MgCl_2$/USY and bulk $MgCl_2$ after five cycles of ammonia absorption/desorption, and after five temperature ramp cycles in the absence of ammonia. As shown in Fig. 12, the NH_3-cycled sample exhibits a decrease in the $MgCl_2$ diffraction peak at 15° 2θ. Additionally, new peaks appear at 32–33° 2θ. The diffraction pattern of the material subjected only to temperature ramps remains the same as that of the fresh sample, indicating that no structural changes occur during thermal cycling alone. This is consistent with the BT analysis, which shows a 5% capacity loss after thermal cycling but a nearly 18% decrease after five ammonia absorption/desorption cycles. The diffraction peaks of the USY phase are not significantly altered by NH_3 sorption cycling.

Because the diffraction peaks of $MgCl_2$ in $MgCl_2$-impregnated USY are of low intensity, it is challenging to observe its structural degradation during cycling. To gain mechanistic insight, bulk $MgCl_2$ was analysed under analogous conditions, which allows us to isolate the effects of temperature and ammonia. Although bulk $MgCl_2$ is not quantitatively equivalent to $MgCl_2$/USY, the observed trends can provide insight into the mechanism of structural change. As shown in Fig. 13, bulk $MgCl_2$ retains its sharp, well-defined peaks after five temperature ramps under argon, confirming high crystallinity and thermal stability in the absence of reactive gases. In contrast, repeated ammonia absorption and desorption cycling induces noticeable changes in peak intensity and broadening. Additionally, new weak diffraction peaks appear in the cycled sample (32–33, 45°2θ), which cannot be attributed to ammoniated species or oxygen species; this is also consistent with the XRD and XPS analysis of the $MgCl_2$/USY sample. These additional peaks most likely originate from secondary crystalline domains, due to the formation of defect-rich $MgCl_2$ polytypes or nanocrystalline interfacial phases. These observations in bulk $MgCl_2$ suggest that structural and crystallinity changes originate from lattice expansion and contraction associated with ammine complex formation and decomposition, rather than from thermal cycling alone. SEM images of bulk $MgCl_2$ before and after ammonia cycling (Fig. S13) show that the overall morphology is largely preserved. Minor surface roughening and particle rearrangement are observed, consistent with volume expansion and contraction during ammonia cycling. Furthermore, EDS analysis (Fig. S14) confirms the absence of ammonia after cycling. Similar processes are likely occurring in $MgCl_2$/USY, although the magnitude may differ due to the presence of the support. Layered $MgCl_2$ is known to accommodate stacking faults and polytypic variants, and stacking faults have been documented in β-$MgCl_2$, resulting in weak additional diffraction peaks [44].

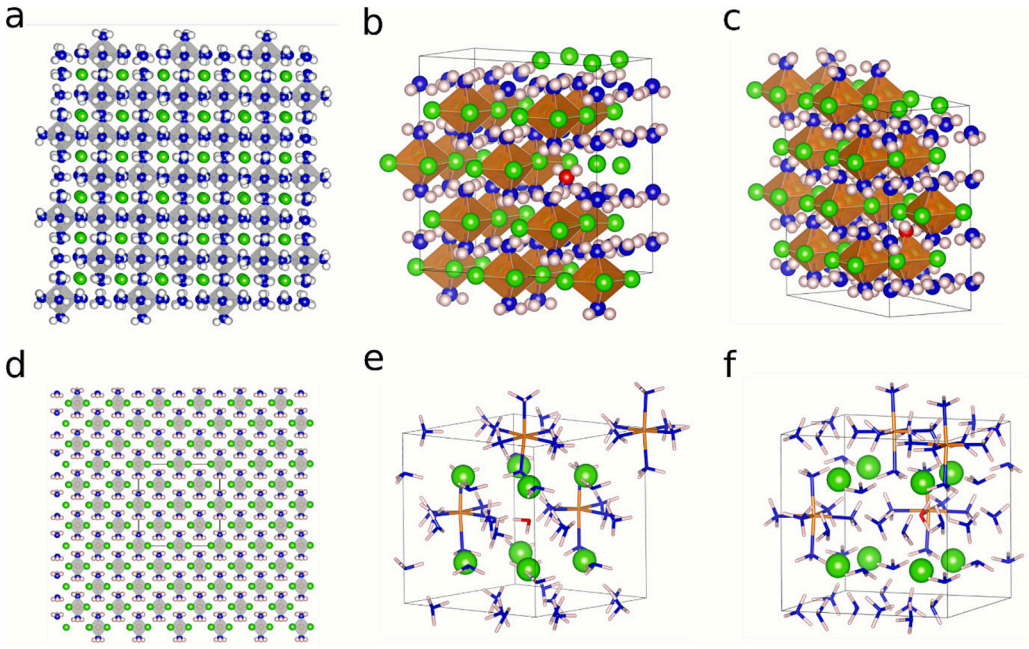

Fig. 9. Structures of a) pristine $MgCl_2 \bullet 6\ H_2O$, b) with one intercalated H_2O molecule and c) one NH_3 substituted for a H_2O molecule. Analogously, d) pristine $MgCl_2 \bullet 2\ H_2O$, e) with one intercalated H_2O, and f) one NH_3 substituted for H_2O.

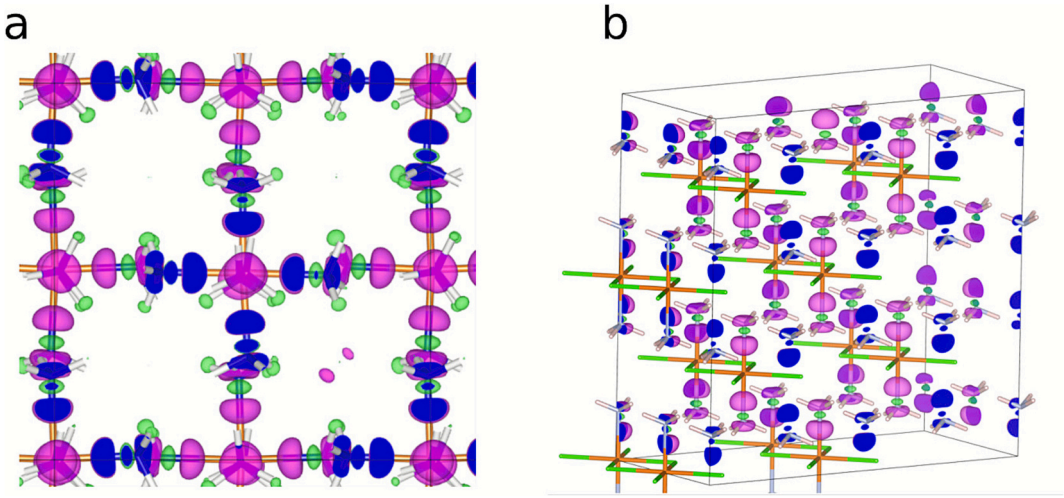

Fig. 10. Charge density difference of a) pristine $MgCl_2$•6 H_2O and b) pristine $MgCl_2$•2 H_2O upon absorption of NH_3.

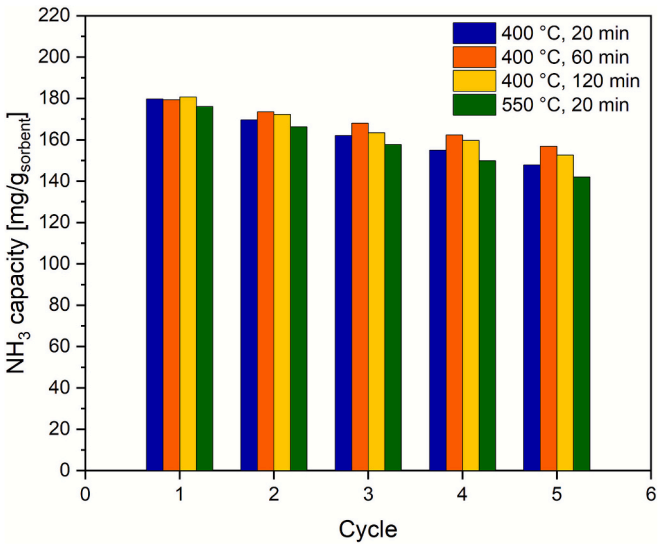

Fig. 11. Ammonia absorption capacity of $MgCl_2$/USY over 5 cycles under different regeneration conditions.

Importantly, the structural defects observed in $MgCl_2$ help define a mechanism that likely contributes to the decrease in ammonia sorption capacity upon cycling, as also reported in other studies [45]. Under the regeneration conditions used in this study, ammonia desorption is reversible. However, the $MgCl_2$/USY sorbent is not fully restored to its initial active state. Residual deactivated domains are observed in $MgCl_2$/USY after regeneration, consistent with the presence of defect-rich $MgCl_2$ phases. These observations suggest that ammonia-induced structural changes are only partially reversible.

Structural changes are also closely linked to the kinetics of ammonia absorption. Breakthrough measurements show improved kinetics after the first ammonia cycle (Fig. S7), which can be attributed to the structural activation of $MgCl_2$. As reported by Aoki et al. [46], this enhancement arises from changes in the structural properties of the ammine complexes following the formation of a disordered state, such as lattice distortion. Cycling introduces structural changes that likely enhance the accessibility of Mg^{2+} coordination sites. This is in accordance with the findings of Takasu et al. [47], who demonstrated superior absorption reactivity through activation of $MgCl_2$ with ammonia prior to sorption.

3.2.2. *High-temperature ammonia absorption*

Understanding the performance of ammonia sorbents under realistic operating conditions is crucial for their potential industrial application. The sorption capacities of the material were measured across a range of temperatures and pressures to evaluate ammonia sorption under conditions closer to those of ammonia synthesis. Future integration of sorbents directly into ammonia synthesis reactors would require them to remain effective even at elevated temperatures. These measurements provide an initial understanding of how pressure influences sorption capacity and help identify the pressure-temperature regions in which sorbent-based separation may offer benefits.

The results show the expected decrease in sorption capacity with increasing temperature and an increase with increasing pressure (Table 2), due to the thermodynamic nature of the gas-solid interaction. This behaviour is consistent with the exothermic nature of ammonia absorption, as higher temperatures shift the equilibrium towards desorption. The capacity rapidly diminishes as the absorption temperature increases. For example, at 8 bar, the sorbent exhibited an ammonia capacity of 239 $mg/g_{sorbent}$ at 50 °C, which dropped significantly to 65 $mg/g_{sorbent}$ at 300 °C. Conversely, increasing the ammonia partial pressure shifts the equilibrium towards higher ammonia loading. At low pressure (Fig. 14), sorption differences between temperatures are more pronounced, whereas at higher pressures, the capacity loss due to temperature is partially compensated by the increased ammonia partial pressure. To assess the potential contribution of the USY support to the measured ammonia capacity, the ammonia capacity of pristine USY was measured at 1 bar and 25 °C. The ammonia uptake was 2 mg/g, which is negligible compared to the 180 $mg/g_{sorbent}$ measured for $MgCl_2$/USY under identical conditions. Consequently, the contribution of USY does not meaningfully influence the calculated coordination number.

Despite the reduction in ammonia capacity at higher temperatures, the measurable capacity at 300 °C is noteworthy and comparable with the existing literature [48]. This result defines an operational window in which $MgCl_2$/USY retains relevant ammonia sorption capacity under conditions that align with emerging concepts for the integrated ammonia synthesis and separation process [13]. This suggests potential for implementation in in-situ ammonia separation, where higher absorption temperatures enable ammonia separation and reduce cooling requirements.

At the same time, this operating window is subject to significant stability constraints. Cyclic sorption and structural analyses reveal that repeated exposure to ammonia induces partially irreversible interfacial defect-rich domains, which gradually reduce the number of active $MgCl_2$ sites. These findings highlight that, although high-temperature operation is feasible, long-term performance depends on the extent of

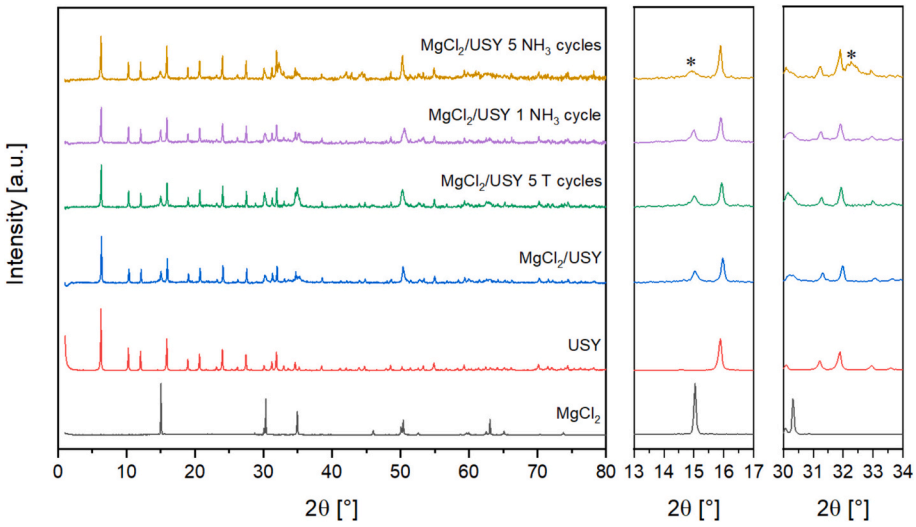

Fig. 12. XRD patterns of fresh $MgCl_2$, USY and $MgCl_2$/USY, and $MgCl_2$/USY after 5 temperature cycles up to 400 °C, $MgCl_2$/USY after 5 temperature cycles and 1 cycle of ammonia absorption/desorption, and $MgCl_2$/USY after 5 cycles of NH_3 absorption/desorption at 400 °C. The symbol (✽) marks the appearance of new peaks or change in the intensity.

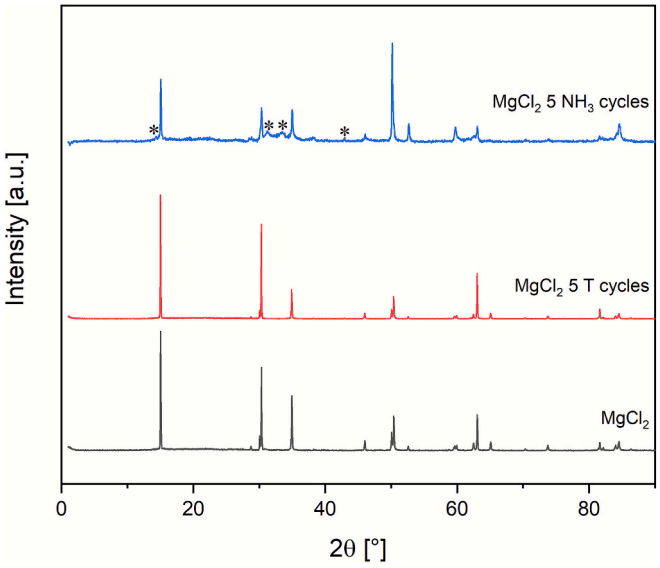

Fig. 13. XRD patterns of fresh $MgCl_2$, $MgCl_2$ after 5 temperature cycles up to 400 °C, and $MgCl_2$ after 5 cycles of NH_3 absorption and desorption at 400 °C. The symbol (✽) marks the appearance of new peaks.

Table 2
Ammonia sorption capacity and coordination number of $MgCl_2$-impregnated USY under different temperatures and pressures.

T_{abs}	p_{abs} [bar]	$p_{parcNH3}$ [bar]	Capacity [mg/$g_{sorbent}$]	Capacity [mg/g_{salt}]	Coordination number[a] [mol/mol_{salt}]
50	1	0.1	158	315	1.76
	5	0.5	222	442	2.47
	8	0.8	255	507	2.83
150	1	0.1	51	102	0.57
	5	0.5	90	179	1.00
	8	0.8	105	210	1.17
300	1	0.1	8	15	0.08
	5	0.5	57	114	0.64
	8	0.8	65	130	0.73

[a] Coordination number was calculated based on the ICP-OES analysis. The coordination numbers include the contribution of the support.

degradation during repeated cycling.

3.3. *Intrinsic $MgCl_2$ chemistry versus support effects*

The degradation pathways investigated in this work reflect both the intrinsic $MgCl_2$ chemistry and the effects of support confinement. The strong affinity of $MgCl_2$ for H_2O, the formation of hydrolysis products such as MgO and MgOHCl, and the thermodynamically favourable replacement of NH_3 by H_2O are intrinsic properties of $MgCl_2$. These are expected to occur regardless of the support type. Similarly, the competitive binding between NH_3 and H_2O as ligands, observed in the DFT calculations, arises from the coordination chemistry of Mg^{2+}. On the contrary, the absolute sorption capacities and the extent of irreversible structural changes during cycling are influenced by the USY support, which determines the dispersion of $MgCl_2$ and site accessibility. While the degradation mechanisms identified in this study are general to $MgCl_2$-based sorbents, the quantitative performance and stability limits are linked to the USY-supported material.

4. Conclusion

$MgCl_2$ is an effective ammonia sorbent due to its strong and reversible interaction with ammonia, making it a promising candidate for separation and storage applications. $MgCl_2$/USY was synthesised, and several key aspects of its performance were investigated, including the influence of water contamination on ammonia sorption capacity and structural properties, the effect of pre-ammoniation on material stability, and the impact of temperature and ammonia binding on cycling performance. High-temperature and high-pressure measurements were also conducted to evaluate the material's potential for integrated ammonia synthesis-separation processes.

In this study, we highlight the impact of water contamination on the ammonia sorption capacity of $MgCl_2$. The results indicate that sorption capacity decreases with exposure to moisture, particularly at higher relative humidity levels. FTIR analysis confirms that water readily binds to $MgCl_2$ even at moderate humidity (30% RH). The observed loss in capacity can be attributed to the formation of oxygen-containing species in the moisture-exposed samples, such as MgO, MgOHCl, and $Mg(OH)_2$, which were identified by XPS analysis. These phases form during hydrolysis when the sample is heated for dehydration and do not exhibit the chemical behaviour required for effective ammonia binding.

Pre-ammoniation of the sample does not mitigate moisture-induced

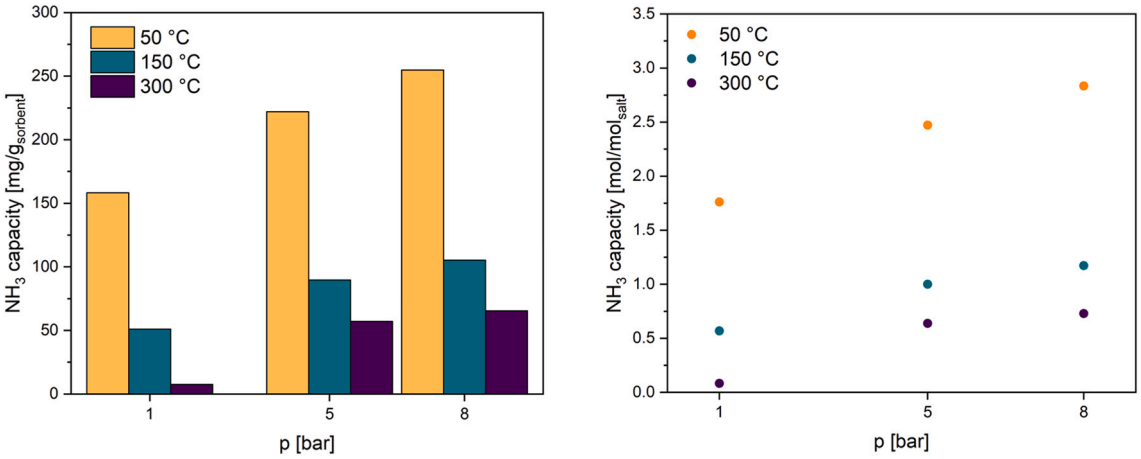

Fig. 14. Ammonia sorption capacity in mg/$g_{sorbent}$ (left) and corresponding coordination number in mol/mol_{salt} (right) of $MgCl_2$/USY at different temperatures (50, 150, and 300 °C) and pressures (1, 5, and 8 bar).

degradation of $MgCl_2$. Instead, in highly pre-ammoniated $MgCl_2$, substitution of NH_3 with H_2O is energetically more favourable. Thermodynamically, ligand exchange is more favourable than water intercalation. Moreover, temperature-programmed desorption results indicate that simultaneous exposure to ammonia and moisture alters the coordination environment of the Mg^{2+} centre, reducing the stability of ammonia complexes. The results demonstrate that pre-ammoniation is ineffective as a protective strategy and that strict moisture control remains essential for mitigating the sorbent performance.

The cycling stability of the material under dry conditions was investigated, as metal halides are known to degrade with repeated use. Using XRD and ammonia sorption capacity measurements on both bulk and USY-impregnated $MgCl_2$, we distinguished the effects of temperature and ammonia on the material's structure and sorption behaviour. Temperature treatment does not cause detectable structural changes, whereas repeated ammonia absorption and desorption induce significant changes. The decline in capacity during cycling is attributed to the formation of secondary crystalline domains associated with defect-rich $MgCl_2$ nanocrystalline interfacial phases, generated by repeated lattice expansion and contraction. These results also indicate that phase transformations induced by ammonia sorption are not fully reversible.

Finally, temperature–pressure measurements show that although ammonia sorption capacity decreases significantly at elevated temperatures, the persistence of measurable uptake of 65 mg/$g_{sorbent}$ at 300 °C and 8 bar is notable. These findings help define the operating window in which sorbent-based separation may be effective and highlight the potential for integrating sorbents directly into ammonia synthesis reactors, where high-temperature absorption could reduce cooling demands while still enabling meaningful ammonia separation performance.

CRediT authorship contribution statement

Aleksandra Zamljen: Writing – original draft, Methodology, Investigation, Formal analysis, Data curation, Conceptualization. **Anže Prašnikar:** Writing – review & editing, Supervision. **Alen Vizintin:** Writing – review & editing, Formal analysis. **Matej Huš:** Writing – review & editing, Writing – original draft, Software, Formal analysis. **Blaž Likozar:** Writing – review & editing, Funding acquisition.

Declaration of competing interest

There are no conflicts to declare.

Acknowledgements

This work was funded by the European Union – Horizon Europe, Grant Agreement [101058643], HySTrAm: Hydrogen Storage and Transport using Ammonia, and by the Slovenian Research and Innovation Agency through core funding P2-0152, infrastructure funding I0-0039, and the research projects N2-0291 and TN-03. The research was (co-)funded under the HyBReED project, supported by the European Union – NextGenerationEU. Computational resources at the HPC system Vega at the Institute of Information Science, Maribor, Slovenia were provided by the HPC RIVR consortium and EuroHPC JU.

Appendix A. Supplementary data

Supplementary data to this article can be found online at https://doi.org/10.1016/j.cej.2026.173423.

Data availability

The data supporting this article are included in the Supplementary Information.

References

[1] D.J. Hrtus, F.H. Nowrin, A. Lomas, Y. Fotsa, M. Malmali, Achieving +95% ammonia purity by optimizing the absorption and desorption conditions of supported metal halides, ACS Sustain. Chem. Eng. 10 (2022) 204–212, https://doi.org/10.1021/acssuschemeng.1c05668.
[2] Y. Kojima, M. Yamaguchi, Thermodynamic analysis of ammonia storage materials, Int. J. Hydrog. Energy 46 (2021) 11756–11760, https://doi.org/10.1016/j.ijhydene.2021.01.070.
[3] A. de Rezende, M. Malmali, P.O. Dral, H. Lischka, D. Tunega, A.J.A. Aquino, Machine learning for designing mixed metal halides for efficient ammonia separation and storage, J. Phys. Chem. C 126 (2022) 12184–12196, https://doi.org/10.1021/acs.jpcc.2c02586.
[4] P.H. Pfromm, Towards sustainable agriculture: fossil-free ammonia, J. Renew. Sustain. Energy 9 (2017), https://doi.org/10.1063/1.4985090.
[5] C. Smith, A.K. Hill, L. Torrente-Murciano, Current and future role of Haber–Bosch ammonia in a carbon-free energy landscape, Energy Environ. Sci. 13 (2020) 331–344, https://doi.org/10.1039/C9EE02873K.
[6] D. Mateo, A. Sousa, M. Zakharzhevskii, J. Gascon, Challenges and opportunities for the photo-(thermal) synthesis of ammonia, Green Chem. 26 (2024) 1041–1061, https://doi.org/10.1039/D3GC02996D.
[7] A. Isella, R. Ostuni, D. Manca, Towards the decarbonization of ammonia synthesis – a techno-economic assessment of hybrid-green process alternatives, Chem. Eng. J. 486 (2024) 150132, https://doi.org/10.1016/j.cej.2024.150132.
[8] S. Lin, X. Zhang, L. Chen, Q. Zhang, L. Ma, J. Liu, A review on catalysts for electrocatalytic and photocatalytic reduction of N 2 to ammonia, Green Chem. 24 (2022) 9003–9026, https://doi.org/10.1039/D2GC03174D.
[9] F.H. Nowrin, M. Malmali, Optimizing reaction-absorption process for lower pressure ammonia production, ACS Sustain. Chem. Eng. 10 (2022) 12319–12328, https://doi.org/10.1021/acssuschemeng.2c03554.

[10] K.H.R. Rouwenhorst, A.G.J. Van der Ham, L. Lefferts, Beyond Haber-Bosch: the renaissance of the Claude process, Int. J. Hydrog. Energy 46 (2021) 21566–21579, https://doi.org/10.1016/j.ijhydene.2021.04.014.
[11] K.H.R. Rouwenhorst, Y. Engelmann, K. van 't Veer, R.S. Postma, A. Bogaerts, L. Lefferts, Plasma-driven catalysis: green ammonia synthesis with intermittent electricity, Green Chem. 22 (2020) 6258–6287, https://doi.org/10.1039/D0GC02058C.
[12] M.J. Palys, A. McCormick, E.L. Cussler, P. Daoutidis, Modeling and optimal design of absorbent enhanced ammonia synthesis, Processes 6 (2018) 91, https://doi.org/10.3390/pr6070091.
[13] C. Smith, L. Torrente-Murciano, Exceeding single-pass equilibrium with integrated absorption separation for ammonia synthesis using renewable energy—redefining the Haber-Bosch loop, Adv. Energy Mater. 11 (2021) 2003845, https://doi.org/10.1002/aenm.202003845.
[14] H. Keestra, Y. Slotboom, K.H.R. Rouwenhorst, D.W.F. Brilman, A century of data: thermodynamics and kinetics for ammonia synthesis on various commercial iron-based catalysts, Chem. Eng. J. 518 (2025) 164593, https://doi.org/10.1016/j.cej.2025.164593.
[15] H. Keestra, K.H.R. Rouwenhorst, D.W.F. Brilman, Universal kinetic model for ammonia synthesis on various ruthenium-based catalysts, Chem. Eng. J. 523 (2025) 168541, https://doi.org/10.1016/j.cej.2025.168541.
[16] Z. Cao, X. Cai, A.C. Feltrin, P. Feng, A. Kaiser, F. Akhtar, Calcium/strontium chloride impregnated zeolite a and X granules as optimized ammonia sorbents, RSC Adv. 12 (2022) 34910–34917, https://doi.org/10.1039/D2RA02981B.
[17] M.J. Kale, D.K. Ojha, S. Biswas, J.I. Militti, A.V. McCormick, J.H. Schott, P. J. Dauenhauer, E.L. Cussler, Optimizing ammonia separation via reactive absorption for sustainable Ammonia synthesis, ACS Appl. Energy Mater. 3 (2020) 2576–2584, https://doi.org/10.1021/acsaem.9b02278.
[18] M. Malmali, G. Le, J. Hendrickson, J. Prince, A.V. McCormick, E.L. Cussler, Better absorbents for ammonia separation, ACS Sustain. Chem. Eng. 6 (2018) 6536–6546, https://doi.org/10.1021/acssuschemeng.7b04684.
[19] B.A. van Hassel, J.R. Karra, J. Santana, S. Saita, A. Murray, D. Goberman, R. Chahine, D. Cossement, Ammonia sorbent development for on-board H2 purification, Sep. Purif. Technol. 142 (2015) 215–226, https://doi.org/10.1016/j.seppur.2014.12.009.
[20] Y. Wang, Y. Shi, D. Xiong, Z. Li, H. Wang, X. Xuan, J. Wang, Metal chloride functionalized MOF-253(Al) for high-efficiency selective separation of ammonia from H2 and N2, Chem. Eng. J. 474 (2023) 145307, https://doi.org/10.1016/j.cej.2023.145307.
[21] Y. Fu, Y. Wu, J. Zeng, S. Wang, X. Li, W. Zhang, H. Ma, Dispersing LiCl in zwitterionic COF for highly efficient ammonia storage and separation, Chem. Eur. J. 29 (2023), https://doi.org/10.1002/chem.202302462.
[22] G.J. Kipouros, D.R. Sadoway, A thermochemical analysis of the production of anhydrous MgCl2, J. Light. Met. 1 (2001) 111–117, https://doi.org/10.1016/S1471-5317(01)00004-9.
[23] Z. Zhang, X. Lu, Y. Yan, T. Wang, The dehydration of MgCl2·6H2O by inhibition of hydrolysis and conversion of hydrolysate, J. Anal. Appl. Pyrolysis 138 (2019) 114–119, https://doi.org/10.1016/j.jaap.2018.12.014.
[24] The Influence of Oxygen Poisoning on A Multiply Promoted Iron Catalyst Used for Ammonia Synthesis: A Temperature-programmed Desorption and Reaction Study, 1997, pp. 111–120, https://doi.org/10.1016/S0167-2991(97)80401-6.
[25] K.C. Waugh, D. Butler, B.E. Hayden, The mechanism of the poisoning of ammonia synthesis catalysts by oxygenates O2, CO and H2O: an in situ method for active surface determination, Catal. Lett. 24 (1994) 197–210, https://doi.org/10.1007/BF00807390.
[26] S.I. Hansen, B.H. Sjølin, I.E. Castelli, T. Vegge, A.D. Jensen, J.M. Christensen, The importance of gas purity in catalytic ammonia synthesis, J. Catal. 450 (2025) 116223, https://doi.org/10.1016/j.jcat.2025.116223.
[27] Q. Huang, G. Lu, J. Wang, J. Yu, Thermal decomposition mechanisms of MgCl2·6H2O and MgCl2·H2O, J. Anal. Appl. Pyrolysis 91 (2011) 159–164, https://doi.org/10.1016/j.jaap.2011.02.005.
[28] G. Kresse, J. Hafner, Ab initio molecular dynamics for liquid metals, Phys. Rev. B 47 (1993) 558–561, https://doi.org/10.1103/PhysRevB.47.558.
[29] G. Kresse, J. Hafner, Ab initio molecular-dynamics simulation of the liquid-metal–amorphous-semiconductor transition in germanium, Phys. Rev. B 49 (1994) 14251–14269, https://doi.org/10.1103/PhysRevB.49.14251.
[30] G. Kresse, J. Furthmüller, Efficiency of ab-initio total energy calculations for metals and semiconductors using a plane-wave basis set, Comput. Mater. Sci. 6 (1996) 15–50, https://doi.org/10.1016/0927-0256(96)00008-0.
[31] G. Kresse, J. Furthmüller, Efficient iterative schemes for ab initio total-energy calculations using a plane-wave basis set, Phys. Rev. B 54 (1996) 11169–11186, https://doi.org/10.1103/PhysRevB.54.11169.
[32] G. Kresse, D. Joubert, From ultrasoft pseudopotentials to the projector augmented-wave method, Phys. Rev. B 59 (1999) 1758–1775, https://doi.org/10.1103/PhysRevB.59.1758.
[33] B. Hammer, L.B. Hansen, J.K. Nørskov, Improved adsorption energetics within density-functional theory using revised Perdew-Burke-Ernzerhof functionals, Phys. Rev. B 59 (1999) 7413–7421, https://doi.org/10.1103/PhysRevB.59.7413.
[34] S. Grimme, J. Antony, S. Ehrlich, H. Krieg, A consistent and accurate ab initio parametrization of density functional dispersion correction (DFT-D) for the 94 elements H-Pu, J. Chem. Phys. 132 (2010), https://doi.org/10.1063/1.3382344.
[35] X. Pan, M. Zhu, H. Mei, Z. Liu, T. Shen, Ammonia absorption enhancement by metal halide impregnated hollow mesoporous silica spheres, ChemistrySelect 5 (2020) 5720–5725, https://doi.org/10.1002/slct.202000965.
[36] X. Tian, J. Qiu, Z. Wang, Y. Chen, Z. Li, H. Wang, Y. Zhao, J. Wang, A record ammonia adsorption by calcium chloride confined in covalent organic frameworks, Chem. Commun. 58 (2022) 1151–1154, https://doi.org/10.1039/D1CC06308A.
[37] H. Ju, Y. Zhang, J. Zhang, Z. Yu, Y. Zhang, X. Zhang, X. Guo, J. Liu, Q. Mao, Q. Liu, Y. Zhao, T. Qi, X. Jiang, Z. Guo, S. Chen, Development of a novel Cu (I) π-complexation adsorbent for ultra-deep desulfurization from a carbon dioxide stream, Smart Molecules 3 (2025), https://doi.org/10.1002/smo.20240027.
[38] S.A. Skaanvik, J.D. Henderson, J.J. Noël, M.C. Biesinger, Speciation of magnesium surfaces by X-ray photoelectron spectroscopy (XPS), Surf. Interface Anal. 57 (2025) 717–728, https://doi.org/10.1002/sia.70003.
[39] F. Tavani, M. Busato, D. Veclani, L. Braglia, S. Mauri, P. Torelli, P. D'Angelo, Investigating the high-temperature water/MgCl 2 interface through ambient pressure soft X-ray absorption spectroscopy, ACS Appl. Mater. Interfaces 15 (2023) 26166–26174, https://doi.org/10.1021/acsami.3c02985.
[40] M. Abazari, R. Jamjah, N. Bahri-Laleh, A. Hanifpour, Synthesis and evaluation of a new three-metallic high-performance Ziegler–Natta catalyst for ethylene polymerization: experimental and computational studies, Polym. Bull. 79 (2022) 7265–7280, https://doi.org/10.1007/s00289-021-03848-x.
[41] X. Pan, M. Zhu, H. Mei, Z. Liu, T. Shen, Ammonia absorption enhancement by metal halide impregnated hollow mesoporous silica spheres, ChemistrySelect 5 (2020) 5720–5725, https://doi.org/10.1002/slct.202000965.
[42] K. Tan, S. Ullah, H. Pandey, E.M. Cedeño-Morales, H. Wang, K. Wang, H.-C. Zhou, J. Li, T. Thonhauser, Competitive adsorption of NH 3 and H 2 O in metal–organic framework materials: MOF-74, Chem. Mater. 34 (2022) 7906–7915, https://doi.org/10.1021/acs.chemmater.2c01637.
[43] Y. Kojima, M. Yamaguchi, Ammonia storage materials for nitrogen recycling hydrogen and energy carriers, Int. J. Hydrog. Energy 45 (2020) 10233–10246, https://doi.org/10.1016/j.ijhydene.2020.01.145.
[44] A. Martorana, A. Marigo, L. Toniolo, R. Zannetti, Stacking faults in the β -form of magnesium dichloride, Z. Krist. 176 (1986) 1–12, https://doi.org/10.1524/zkri.1986.176.1-2.1.
[45] V.E. Sharonov, Y.I. Aristov, Ammonia adsorption by MgCl2, CaCl2 and BaCl2 confined to porous alumina: the fixed bed adsorber, React. Kinet. Catal. Lett. 85 (2005) 183–188, https://doi.org/10.1007/s11144-005-0259-5.
[46] T. Aoki, H. Miyaoka, H. Inokawa, T. Ichikawa, Y. Kojima, Activation on ammonia absorbing reaction for magnesium chloride, J. Phys. Chem. C 119 (2015) 26296–26302, https://doi.org/10.1021/acs.jpcc.5b07965.
[47] H. Takasu, J. Kaneko, S. Yoshida, T. Harada, Y. Kato, Reactivity improvement of magnesium chloride by ammonia pre-coordination for thermochemical energy storage at approximately 100 °C, ISIJ Int. 62 (2022) ISIJINT-2022-136, https://doi.org/10.2355/isijinternational.ISIJINT-2022-136.
[48] S.M.T. Mahtab, M. Malmali, Insights into structure-composition-capacity relationship of ultrastable metal halide absorbents for ammonia separation and storage, Chem. Eng. J. 507 (2025) 160105, https://doi.org/10.1016/j.cej.2025.160105.